

X-ray refraction-enhanced imaging and a method for phase retrieval for a simple object

Yoshio Suzuki, Naoto Yagi* and Kentaro Uesugi

SPRING-8/JASRI, Mikazuki, Hyogo 679-5198, Japan.
E-mail: yagi@spring8.or.jp

Refraction-enhanced imaging is now widely used for imaging low-absorption-contrast specimens in the hard X-ray region. However, the interpretation of the details of a refraction-enhanced image is not always clear. In this paper the theoretical treatment of refraction-enhanced imaging and a method for phase retrieval from refraction-contrast images are discussed in comparison with angular-deflection mapping of the transmitting beam. The problems of thick and complicated objects are also discussed.

Keywords: refraction contrast; phase contrast; phase retrieval; tomography.

1. Introduction

When electromagnetic radiation is propagated through a non-uniform object, the wave front is deformed by the effective path difference of the propagated wave (refraction effects). This phenomenon has been recently applied to visualization of non-absorbing objects in the hard X-ray region (Davis *et al.*, 1995; Snigirev *et al.*, 1995; Wilkins *et al.*, 1996; Cloetens *et al.*, 1996). This effect, from the point of view of geometrical optics, results in the angular deflection of the transmitted beam, and also results in a phase shift of the transmitted wave from the point of view of wave optics.

If the object-to-detector distance is zero, *i.e.* the contact microscopy conditions, no contrast due to the refraction is observed. By setting the detector at an appropriate distance, edge-enhanced images can be observed, as shown in Fig. 1. This contrast-enhancement mechanism due to the refraction effect is the same as that of the Schlieren method in visible light optics. The optical system of the refraction-enhanced imaging is the same as that of Gabor-type holography. In the case of holographic imaging, the image formation must be described by wave optics (Cloetens *et al.*, 1996; Pogany *et al.*, 1997. Phase retrieval based on wave optics (Kirchhoff theory) has

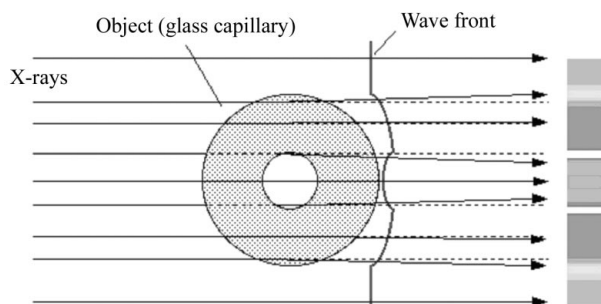


Figure 1

Illustrating the X-ray wave front and trajectories through an object. The direction of the X-rays is slightly deflected at the interfaces in accordance with Snell's law of refraction as in geometrical optics. However, the direction of deflection is not the same as that for visible light, because the refractive index for X-rays is slightly smaller than unity. X-rays are focused by a concave lens, and defocused by a convex lens.

been already carried out by two methods, namely the holographic method (Cloetens, Ludwig, Van Dyck *et al.*, 1999) and the direct solution of a differential equation (Gureyev *et al.*, 1999). On the other hand, refraction-enhanced imaging is just at the transition between wave optics and geometrical optics. The refraction contrast based on geometrical optics has already been discussed in a previous paper (Suzuki *et al.*, 1999). In this paper the contrast-enhancement method and a phase-retrieval method are discussed and compared with experimental results on a refraction-enhanced image and an angular-deflection mapping image.

This refraction-enhanced imaging is very useful in some cases. However, when this method is applied to a thick and complicated specimen there is a serious problem. Overlapping structures cannot be resolved and a one-to-one relation between the object and image is not preserved. In §4 the problems for thick and complicated objects will be discussed by using experimental results on biological samples.

2. Theory of refraction-enhanced imaging based on wave optics

When an object is illuminated by a plane wave, the electric field, $E(x)$, just behind the object may be written as

$$E(x) = \exp[-\beta(x) + i\Phi(x)], \quad (1)$$

where $\beta(x)$ and $\Phi(x)$ represent the absorption and phase shift, respectively. The attenuation of transmitting radiation is represented in a general formula as

$$I = I_0 \exp[-2\beta(x)], \quad (2)$$

where I and I_0 are the intensity of the transmitting and incident beam, respectively. Here, I_0 is assumed to be unity for simplification. Assuming $\beta(x)$, $\Phi(x) \ll 1$, and ignoring higher orders of $\beta(x)$ and $\Phi(x)$, $E(x)$ can be written as

$$E(x) = 1 - \beta(x) + i\Phi(x). \quad (3)$$

The assumption of $\beta(x)$, $\Phi(x) \ll 1$ corresponds to a weak-absorption and small-phase-shift case. Using the Fourier expansion formula, $E(x)$ can be expressed as

$$E(x) = 1 - \sum b_m \exp(ik_m x) + i \sum c_m \exp(ik_m x). \quad (4)$$

The electric field at the image plane, $F(y, r)$, is expressed by using the Kirchhoff integral as follows,

$$F(y, r) = (\lambda r)^{-1/2} \exp(-ikr) \int E(x) \exp[-ik(y-x)^2/(2r)] dx, \quad (5)$$

where r is the object-to-image plane distance and k is a wavevector defined by

$$k = 2\pi/\lambda. \quad (6)$$

By using the expansion formula of (4), the image field is rewritten as

$$F(y, r) = (\lambda r)^{-1/2} \exp(-ikr) \left\{ \int \exp[-ik(y-x)^2/(2r)] dx - \sum b_m \int \exp(ik_m x) \exp[-ik(y-x)^2/(2r)] dx + i \sum c_m \int \exp(ik_m x) \exp[-ik(y-x)^2/(2r)] dx \right\}. \quad (7)$$

Here,

$$(\lambda r)^{-1/2} \exp(-ikr) \left\{ \int \exp[-ik(y-x)^2/(2r)] dx \right\} = 1, \quad (8)$$

because the flux density of the incident radiation is preserved in the case of plane-wave illumination. The second and third terms in (7) can be transformed as

$$\exp(ik_m x) \exp[-ik(y-x)^2/(2r)] = \exp\left\{-ik/(2r)[x - (y + rk_m/k)]^2\right\} \times \exp(-ik_m y) \exp[-irk_m^2/(2k)]. \quad (9)$$

Therefore, $F(y, r)$ can be rewritten as,

$$F(y, r) = 1 - \sum b_m \exp(-ik_m y) \exp[-irk_m^2/(2k)] + i \sum c_m \exp(-ik_m y) \exp[-irk_m^2/(2k)]. \quad (10)$$

When $rk_m^2/(2k) \ll 1$, the exponential term can be substituted by an expansion formula,

$$\exp[-irk_m^2/(2k)] \simeq 1 - irk_m^2/(2k). \quad (11)$$

Then, (10) is rewritten as

$$F(y, r) = 1 - \sum b_m \exp(-ik_m y) + i \sum b_m \exp(-ik_m y) rk_m^2/(2k) + i \sum c_m \exp(-ik_m y) + \sum c_m \exp(-ik_m y) rk_m^2/(2k). \quad (12)$$

The modulation of the electric field due to the refraction effect can be defined by

$$\Delta F(y) \equiv F(y, r) - F(y, 0), \quad (13)$$

where, $F(y, 0) = E(x)$ is the electric field just behind the object,

$$F(y, 0) = 1 - \sum b_m \exp(-ik_m y) + i \sum c_m \exp(-ik_m y). \quad (14)$$

The third and fifth terms in (12) can be rewritten as follows,

$$i \sum b_m \exp(-ik_m y) rk_m^2/(2k) = ir/(2k) \left\{ \partial^2 \left[- \sum b_m \exp(-ik_m y) \right] / \partial y^2 \right\}, \quad (15)$$

and

$$\sum c_m \exp(-ik_m y) rk_m^2/(2k) = ir/(2k) \left\{ \partial^2 \left[i \sum c_m \exp(-ik_m y) \right] / \partial y^2 \right\}. \quad (16)$$

Finally, the electric field at the image plane can be derived from the electric field at the object plane as follows,

$$F(y, r) = F(y, 0) + ir/(2k) \left[\partial^2 F(y, 0) / \partial y^2 \right]. \quad (17)$$

When the absorption is negligibly small, *i.e.* a pure phase object, then $\beta(x) = 0$. Then the intensity profile at the image plane, $I(y)$, can be expressed by

$$I(y, r) = |F(y, r)|^2 \simeq |F(y, 0)|^2 + r/k \left[\partial^2 \Phi(y, 0) / \partial y^2 \right], \quad (18)$$

where $\Phi(y, 0)$ corresponds to the wave front form just behind the object $\Phi(x)$ in the case of plane-wave illumination. Consequently, the intensity modulation due to the refraction is simply described by the second derivative of the phase. This formula is valid for the case of negligibly small absorption and weak phase shift, and $rk_m^2/(2k) \ll 1$. A similar result has previously been obtained under somewhat more general conditions, *i.e.* not requiring a weak phase shift, by Cowley (1975) and Teague (1983). When the minimum structure of the object is Δx , then $1/\Delta x$ corresponds to the spatial frequency k_m , as $k_m \simeq 2\pi/\Delta x$. The term $(\lambda r)^{1/2}$ represents the blurring of the image due to Fresnel diffraction. The condition $rk_m^2/(2k) \ll 1$ can be expressed as

$$\lambda r \ll 4\pi(\delta x/2\pi)^2. \quad (19)$$

The above condition is fully satisfied when $(\lambda r)^{1/2} \simeq \Delta x/2\pi$, which corresponds to the condition for which geometrical optics are a good approximation, *i.e.* the broadening due to the Fresnel diffraction is smaller than the lateral structure of the object. Then the edge-enhanced image can be observed with little deterioration of the spatial resolution, and the macroscopic structure of the object is preserved in the projection image.

The modulation of the intensity due to the refraction can be evaluated by assuming a typical sample structure. When the thickness of the sample has a sinusoidal form, given by $t \sin(k_m x)$, the wave front is expressed by

$$\Phi(x) = 2\pi\delta t/\lambda \sin(k_m x), \quad (20)$$

where δ is defined by $\delta = 1 - n$ (where n is the index of refraction). If the spatial resolution of the imaging apparatus is better than $1/k_m$, the intensity modulation is not degraded by the finite resolution of the optical system. Therefore, when $(\lambda r)^{1/2} \simeq \Delta x/2\pi$, the intensity modulation can be expressed by using equation (18) as follows (Cloetens *et al.*, 1996; Pogany *et al.*, 1997),

$$\begin{aligned} I(y, r) - |F(y, 0)|^2 &= -(2\pi/\lambda)r/k\delta t k_m^2 \sin(k_m x) \\ &\simeq -\delta t/\lambda \sin(k_m x) \\ &= -\Phi(x)/2\pi. \end{aligned} \quad (21)$$

This result is essentially the same as the contrast-enhancement formula based on geometrical optics (Suzuki *et al.*, 1999).

The deflection angle, $\theta(y)$, of the transmitted beam due to the refraction is written as

$$\theta(x) = \partial\Phi(x)/\partial x, \quad (22)$$

because the propagation vector is normal to the wave front.

Although the above formulae are only one-dimensional, it is apparent that they can be expanded into two-dimensional forms,

$$\Delta I = r/k \nabla^2 \Phi, \quad (18')$$

and

$$\Delta k = \nabla \Phi. \quad (22')$$

3. Phase retrieval from a refraction-enhanced image and angular-deflection image

Phase retrieval can be performed by either angular-distribution mapping or intensity mapping. As is apparent from equation (22), when the angular deflection $\theta(y)$ is measured the phase mapping is derived by an integral of $\theta(y)$, namely

$$\Phi(y) = \int \theta(y) dy. \quad (23)$$

When the intensity-modulated image is measured, the phase mapping can be obtained by solving equation (18). For the case of a one-dimensional object, the method becomes much simpler. The phase mapping can be obtained by a second integral of the normalized image as follows,

$$\Phi(y) = \iint k/r [I(y) - I_0]/I_0 dy^2, \quad (24)$$

where $I_0 = |F(y, 0)|^2$ is the flux density at the image plane without an object. It is apparent from (23) and (24) that the deflection-angle mapping is derived by the integral of the refraction-enhanced image,

$$\theta(y) = \int k/r [I(y) - I_0]/I_0 dy. \quad (25)$$

An experiment on phase retrieval has been attempted by using a model sample with a simple structure in order to confirm the feasibility for measured data. The experiment was performed at undulator beamline 47XU at SPring-8. A schematic diagram of the beamline and experimental set-up is shown in Fig. 2. The X-ray beam, monochromated by passing through an Si(111) double-crystal monochromator, was extracted into the experimental hutch. The projection images were recorded using a two-dimensional detector set far from the specimen. The distance between the sample and detector was

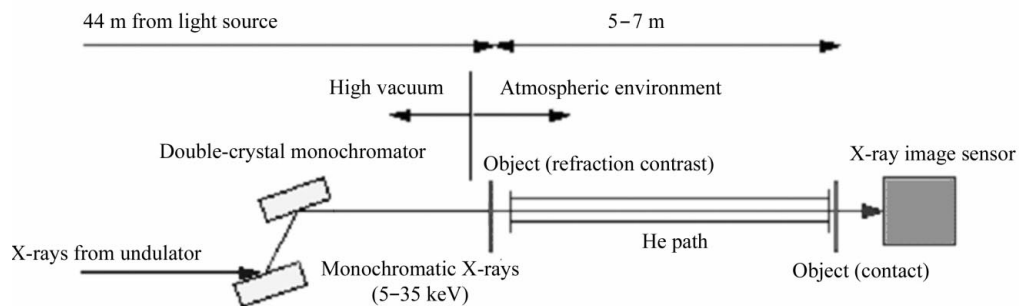


Figure 2
Schematic diagram of the experimental set-up at BL47XU of SPring-8.

6.5 m for the refraction contrast. The field of view was about 3 mm × 3 mm in the experiment. The image detector used for the experiment was an indirect-sensing X-ray image sensor that consisted of a CCD camera (Hamamatsu Photonics C4880-17), thin (about 10 μm) phosphor screen (P43: Gd-O-S) and 1:1 relay lens system. The format of the CCD consisted of 1000 × 1018 pixels of 12 μm × 12 μm pixel size. The measured spatial resolution of the image detector was estimated to be about 20 μm (~2 pixel width). Details of the experiment have already been described elsewhere (Suzuki *et al.*, 1999).

The model sample was a glass capillary with 660 μm outer diameter and 220 μm inner diameter. The measured projection image of the sample is shown in Fig. 3, and the intensity profile is shown in Fig. 4. A pair of bright and dark lines are observed at the boundaries between the glass and air.

The deflection of the transmitted beam was also measured using a fine X-ray beam collimated by a slit (width 20 μm). The lateral shift of the transmitted beam position was monitored using the CCD camera situated 6.5 m from the object. The sample was scanned across the capillary axis to measure the beam displacement at each point of incidence. Measured data are 50 images by a 20 μm step. The positional shift of the transmitted beam through the capillary was around 10 μm on the image plane. Least-mean-square curve fitting was used to derive the beam centre for each measured image. The measured

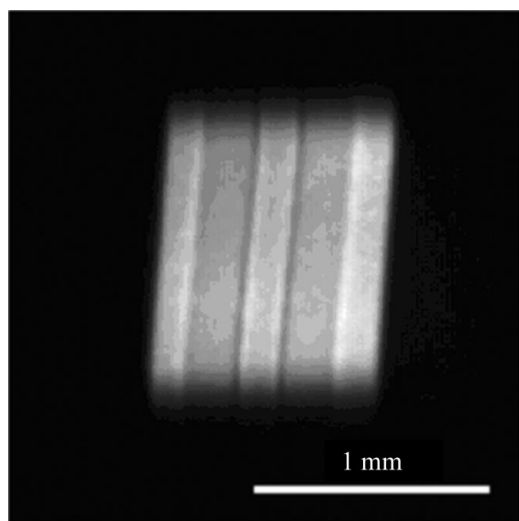


Figure 3
Refraction-contrast image of a glass capillary. X-ray energy: 28.8 keV. Object-to-detector distance: 6.5 m.

deflection angles are shown in Fig. 5. A strong beam deflection at the boundary between air and glass is clearly observed.

The phase mapping was derived from the measured intensity profile or from the measured deflection-angle mapping. The deflection-angle mapping, reconstructed by using equation (25) from the measured intensity profile, is shown in Fig. 6(a), and the reconstructed phase mapping by using equation (24) is shown in Fig. 6(b). The calculated angular

profile shows good agreement with the measured angular deflection in Fig. 5, except for some broadening. The blurring is caused by a lack of spatial resolution of the imaging detector and by the long working distance between the object and detector. The reconstructed phase mapping qualitatively agrees with the shape of the sample. The phase

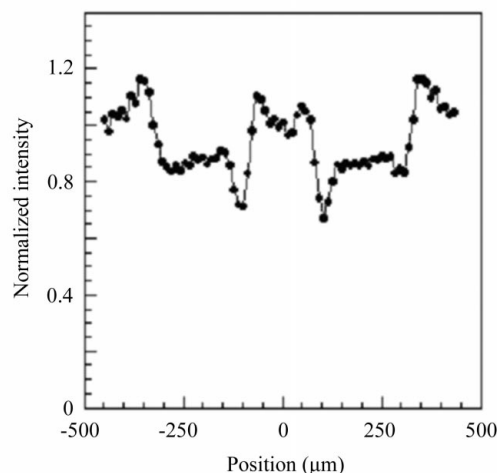


Figure 4
Intensity profile of the refraction-contrast image in Fig. 3. The sample is a glass capillary (660 μm outer diameter and 220 μm inner diameter).

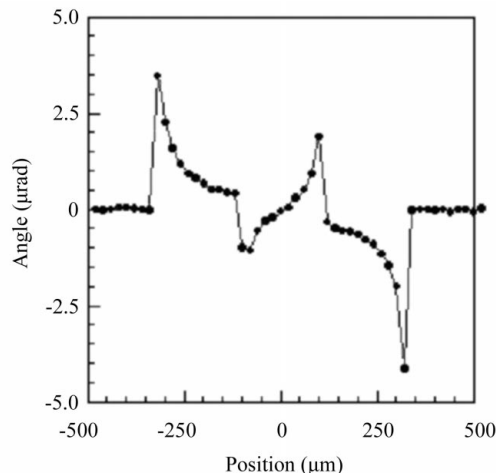


Figure 5
Angular deflection of the transmitted beam. Solid circles: experimental data.

retrieval from the measured angular deflection by using equation (23) is shown in Fig. 7. The phase profile agrees well with the shape of the object. Compared with the phase image derived from the deflection-

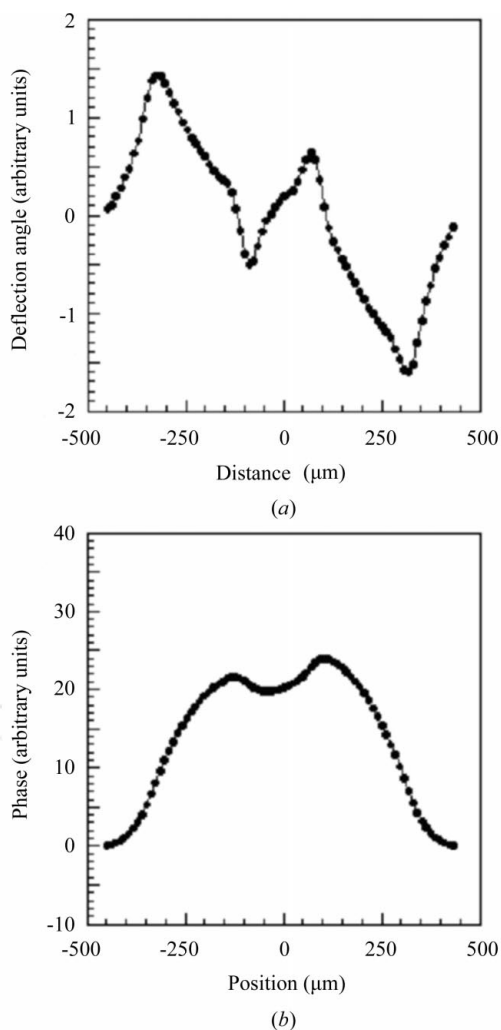


Figure 6
(a) Reconstructed deflection-angle profile derived from the refraction-contrast image profile shown in Fig. 4. (b) Reconstructed phase mapping derived from this profile.

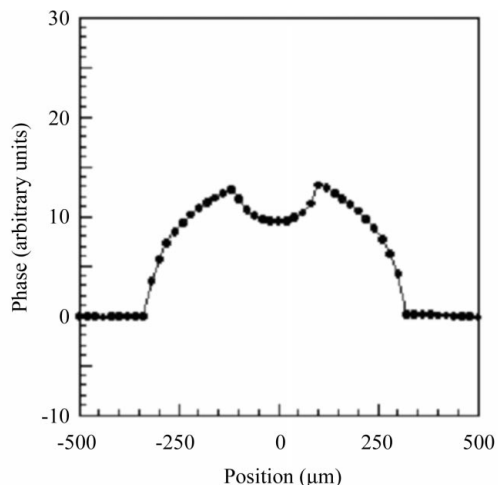


Figure 7
Reconstructed phase profile derived from the angular-deflection mapping shown in Fig. 5.

angle measurement, the phase image retrieved from the refraction-enhanced image is apparently deformed. This is considered to be due to the lack of spatial resolution of the imaging system. The sample-to-detector distance of 6.5 m is probably too long in order to satisfy the condition (19).

4. Refraction contrast for thick and complicated objects: lung as an example

Although phase can be retrieved from an image dominated by refraction as shown above, such a technique can be applied only for limited types of images. In practice, images from real objects are much more complicated. Here we give some examples of lung images from various animals.

A lung of a mouse gives a splendid refraction-contrast image (Yagi *et al.*, 1999). A lung of a rat also gives a good image provided that adequate X-ray energy and specimen-to-detector distance are used. An example is shown in Fig. 8(b), recorded using 35 keV X-rays at 5.5 m. Compared with a contact image (Fig. 8a), the amount of available information in the image is much larger. When the beam energy is lowered to 20 keV, the image became blurred (Fig. 9). This happens when the bright edge caused by refraction becomes too broad: at lower energy, deflection of the beam due to refraction is larger. Since the refraction contrast is made by edge enhancement, an

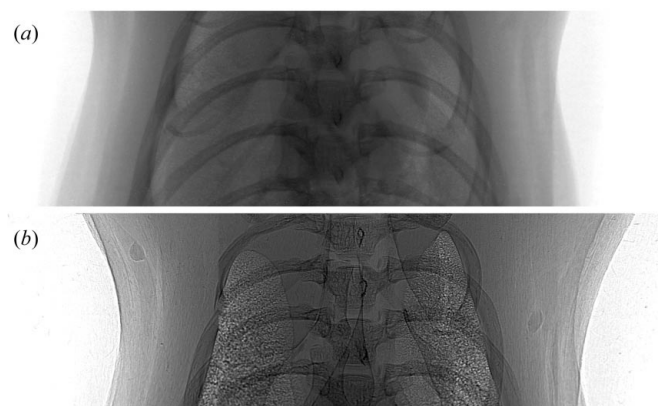


Figure 8
Images of thorax of a hairless rat. The X-ray energy was 35 keV. The images were obtained with the detector (a) close to the sample and (b) at 5.5 m from the sample. These images were recorded at BL20B2 of SPring-8, which is a bending-magnet beamline. The experimental station was about 200 m from the X-ray source. The detector was Beam Monitor 4, which consisted of a 10 μm -thick phosphor (P43), tandem lens system ($f = 105$ mm, $F = 2.4$) and a cooled CCD camera (Hamamatsu Photonics, C4880-31-24A with 1024×1024 24 μm pixels). The exposure was 30 s. In (b), bronchi and lung are visualized clearly. The width of the chest was about 36 mm. The rat was killed by an overdose of pentobarbital.

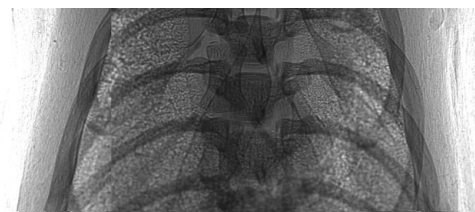


Figure 9
Image of thorax of a hairless rat taken with 20 keV X-rays and a specimen-to-detector distance of 5.5 m. The other conditions are the same as in Fig. 8.

image loses resolution when the fringe is too wide. On the other hand, at higher energy (51 keV, Fig. 10), finer fringes give higher resolution but the contrast is lower than at 35 keV. On closer examination, it can be observed that the image of the lung is made of bright and dark dots. Thus the choice of beam energy and distance is quite important, as has already been discussed (Cloetens *et al.*, 1997; Pogany *et al.*, 1997). It is also important to choose an adequate detector resolution.

The thickness of a lung depends on the part of the lung used, but it is at least a few millimetres in a rat. Considering that the size of an alveolus is 100–200 μm , there must be a few tens of alveoli superimposed in the image. Usually, when so many objects are overlapping in a view, the contrast decreases. However, the image in Fig. 8(b) has a very good contrast. It should be noted that this does not mean each alveolus can be resolved. It is indeed very improbable that each alveolus can be seen even when the specimen is thinner, like a mouse lung, unless it is in a single layer. Thus it is surprising that high contrast is achieved with a rat lung. The cause of the contrast seems to be multiple refraction of the beam. X-rays that are refracted by one layer of alveoli are refracted again in the next layer. This seems to give rise to spots with high and low intensities in the image. The precise mechanism with which high contrast is created by multiple layers of alveoli has to be studied physically, using a test sample.

When the specimen is very thick, the image becomes featureless. Fig. 11 is a refraction-contrast image of the chest of a rabbit. This image was recorded with the same X-ray energy as that used for Fig. 10 but with about twice the specimen-to-detector distance. Since the width of a fringe is proportional to the distance and inversely

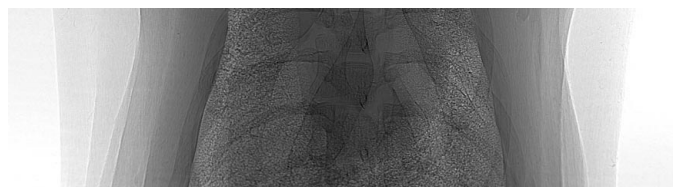


Figure 10
Image of thorax of a hairless rat taken with 51 keV X-rays and a specimen-to-detector distance of 5.5 m. The other conditions are the same as in Fig. 8.

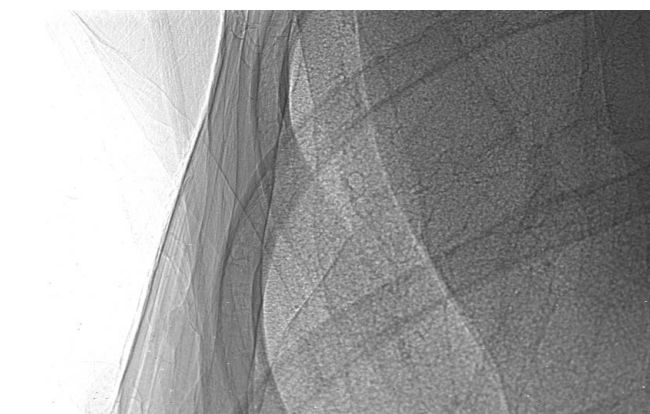
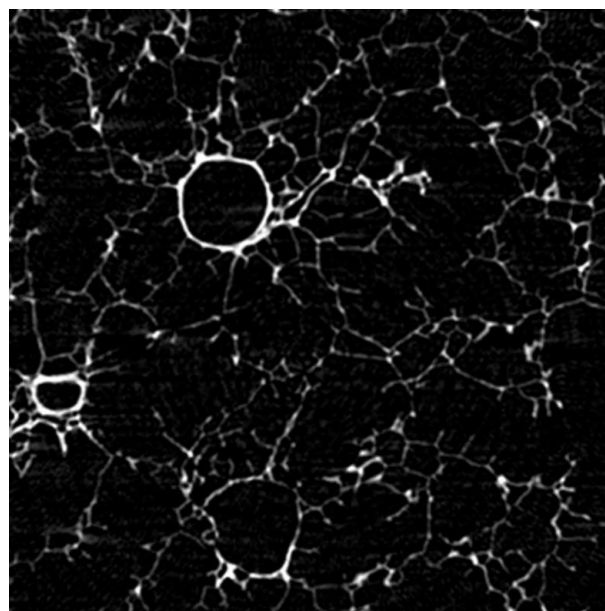
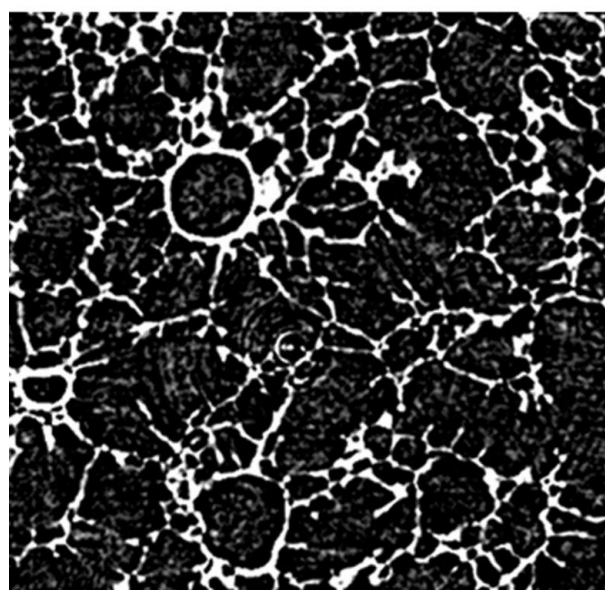


Figure 11
Image of thorax of a skinned rabbit taken with 51 keV X-rays and a specimen-to-detector distance of 12 m. The exposure time was 60 s. The width of the image is 24 mm. The other conditions are the same as in Fig. 8. The rabbit was killed by an overdose of pentobarbital and its fur was removed with the skin. The dark region on the right is probably the heart containing a large amount of blood.

proportional to the square of the X-ray energy, the image is expected to resemble that of Fig. 8(b), which has a good contrast. However, the major part of the lung, which is made of bronchi and alveoli, looks fairly smooth with weak contrast. This is most probably because overlapping of too many refracting objects caused averaging of features. The most pronounced features are due to wrinkles on the body surface (lines running more or less vertically).



(a)



(b)

Figure 12
Tomographic reconstructions of a cross section of a chemically fixed human lung (a Heitzman preparation, courtesy of Professor J. Ikezoe and Dr K. Shimizu). (a) Image obtained by a conventional tomography technique using absorption contrast (specimen-to-detector distance: 5 cm). (b) Image obtained by using refraction contrast (specimen-to-detector distance: 50 cm). Both reconstructions were calculated from images recorded at BL20B2 of SPring-8, using Beam Monitor 2 and a cooled CCD camera (Hamamatsu C4880-10-24A, 1000×1018 pixels). The actual size is about 4 mm square.

This averaging effect is important when one considers practical applications of refraction-enhanced imaging. Although good contrast can be obtained with a fairly thick sample (*e.g.* rat lung), interpretation of an image is difficult when the image is made of dots. The many small bright and dark dots do not correspond to any real structure. When the object is thicker, the image becomes featureless. Thus, in the case of projection imaging of a lung, the best application will be on small animals such as mice. Phase retrieval from a simple projection image, as described in this paper, may only be possible when the thinnest part of an edge of mouse lung is chosen as the object.

One obvious way to circumvent the problem of overlapping is to use a tomographic technique. Synchrotron radiation tomography can provide a high-resolution three-dimensional structure (Bonse & Busch, 1996; Salome *et al.*, 1999). However, this technique has problems when applied to biological samples. One is a practical limitation that the exposure time tends to be of the order of minutes or hours. Since the images shown above were recorded from lungs of dead animals, it was not necessary to record them in a short exposure. However, most important applications require observation of a lung in live animals. Thus, ideally the exposure time should be shorter than 1 s. Moreover, even with lungs of dead animals, tomographic experiments are difficult because the shape of lungs tends to change in a prolonged exposure. Thus, it is generally impractical to apply a tomographic technique for high-resolution imaging of lungs.

As for tomography using refraction enhancement, we found that increased noise degrades the quality of a reconstructed image. Fig. 12(a) shows a tomographic reconstruction of a cross section of a chemically fixed human lung (sample courtesy of Professor Ikezoe and Dr Shimizu of Ehime University Medical School). This image was obtained using a conventional transmission tomography technique for which the specimen was placed close to the detector. Fig. 12(b) shows the same section obtained with a specimen-to-detector distance of 50 cm. The same reconstruction program as used for Fig. 12(a) was used to obtain the cross section. Owing to the refraction at the edges of the alveolar walls, the contrast is improved. However, there are numerous contrast features within alveoli where no density is expected. These artifacts appear at the crossing points of the intense refracted X-rays. Although the alveolar walls are visualized with a better contrast, the artifacts in the background make it necessary to raise the cut-off level for the display. However, when this

is done, the clear bright contrast at the edges of the alveolar walls diminishes, making the image similar to that obtained using a standard technique. When the high contrast is lost, the image suffers from low spatial resolution caused by the broadening of the lines delineating the surfaces of the alveolar walls.

Thus, the refraction-enhanced tomography of the lung does not seem to improve an image obtained using the conventional technique. Use of a holographic tomography technique (Cloetens, Ludwig, Baruchel *et al.*, 1999), which effectively performs a phase retrieval, may provide more useful information. However, since the contrast in the images obtained using a conventional tomography technique is good enough (Fig. 12a), the holographic technique, which is best applied to specimens with a low density contrast, will probably not be effective in the imaging of lungs.

References

- Bonse, U. & Busch, F. (1996). *Prog. Biophys. Mol. Biol.* **65**, 133–169.
- Cloetens, P., Barrer, R., Baruchel, J. D., Guigay, J. P. & Schlenker, M. (1996). *J. Phys. D*, **29**, 133–146.
- Cloetens, P., Ludwig, W., Baruchel, J., Van Dyck, D., Van Landuyt, J., Guigay, J. P. & Schlenker, M. (1999). *Appl. Phys. Lett.* **75**, 2912–2914.
- Cloetens, P., Ludwig, W., Van Dyck, D., Guigay, J. P., Schlenker, M. & Baruchel, J. (1999). *Proc. SPIE*, **3772**, 279–290.
- Cloetens, P., Pateyron-Salome, M., Buffiere, J. Y., Peix, G., Baruchel, J., Peyrin, F. & Schlenker, M. J. (1997). *J. Appl. Phys.* **81**, 5878–5886.
- Cowley, J. M. (1975). *Diffraction Physics*, p. 61. Amsterdam: North Holland.
- Davis, T. J., Gao, D., Gureyev, T. E., Stevenson, A. W. & Wilkins, S. W. (1995). *Nature (London)*, **373**, 595–598.
- Gureyev, T. E., Raven, C., Snigirev, A., Snigireva, I. & Wilkins, S. W. (1999). *J. Phys. D*, **32**, 563–567.
- Pogany, A., Gao, D. & Wilkins, S. W. (1997). *Rev. Sci. Instrum.* **68**, 2774–2782.
- Salome, M., Peyrin, F., Cloetens, P., Odet, C., Laval-Jeantet, A. B., Baruchel, J. & Spanne, P. (1999). *Med. Phys.* **26**, 2194–2204.
- Snigirev, A., Snigireva, I., Kohn, V., Kuznetsov, S. & Schelokov, I. (1995). *Rev. Sci. Instrum.* **66**, 5486–5492.
- Suzuki, Y., Yagi, N., Umetani, K., Kohmura, Y. & Yamasaki, K. (1999). *Proc. SPIE*, **3770**, 13–22.
- Teague, M. R. (1983). *J. Opt. Soc. Am.* **73**, 1434–1441.
- Wilkins, S. W., Gureyev, T. E., Gao, D., Pogany, A. & Stevenson, A. W. (1996). *Nature (London)*, **384**, 335–338.
- Yagi, N., Suzuki, Y., Umetani, K., Kohmura, Y. & Yamasaki, K. (1999). *Med. Phys.* **26**, 2190–2193.